東北大学機関リポジトリ
TOUR
Tohoku University Repository

東北大学

(e, e + ion) study on electron-induced dissociative ionization of O2

$(e, e + \text{ion})$ study on electron-induced dissociative ionization of O_2

Noboru Watanabe,[*] So Yamada, and Masahiko Takahashi

Institute of Multidisciplinary Research for Advanced Materials, Tohoku University, Sendai 980-8577, Japan

Electron-induced dissociative ionization of O_2 has been investigated by means of $(e, e + \text{ion})$ spectroscopy. The linear momenta of the fragment ions have been measured in coincidence with electron energy-loss spectra for O_2 at scattering angles of $2.2°$, $4.2°$, and $8.2°$ using an incident energy of 1.4 keV. From the analysis of the data, partial ion yield spectra have been obtained for the $B\,^2\Sigma_g^-$, $\{c\,^4\Sigma_u^- + 2\,^2\Sigma_u^- + 2\,^4\Sigma_u^-\}$, $\{2\,^2\Sigma_u^- + 2\,^4\Sigma_u^-\}$, and $3\,^2\Sigma_u^-$ ionization, allowing us to assess state-specific momentum-transfer dependence of the relative ionization cross sections. It has been shown that the shape resonance in the $B\,^2\Sigma_g^-$ channel is substantially suppressed by the contributions of electric nondipole transitions. To get insight into the stereodynamics in the electron-O_2 collision processes, the angular distributions of the fragment ions have been examined. It has been revealed that the $(e, e + \text{ion})$ cross section for the $2\sigma_g \to 1\pi_g$ autoionization band exhibits a characteristic angular distribution reflecting the anisotropic shape of the molecular orbital to which the target electron is excited.

I. INTRODUCTION

Electron-induced dissociative ionization of molecules is a fundamental process in collision physics and molecular physics. In electron-impact ionization, a portion of the incident electron energy is transferred to the target and distributed among the internal energy of the molecular ion and the kinetic energy of the ejected electron. The molecular cation may, if the internal energy is sufficiently high, decay into ionic and neutral fragments. Dissociative ionization occurs also via photoionization, but there is an essential difference between the photo- and electron-induced processes, where the latter is not restricted by the dipole selection rules and electric quadrupole and higher multipole transitions contribute to the reaction, depending upon the magnitude of momentum transferred from the incident electron to the target.

The dissociative ionization of molecular oxygen is an important source of energetic fragment species that play crucial roles in physical and chemical processes in planetary atmospheres and laboratory plasmas [1]. To get detailed knowledge of the dissociative ionization of O_2, various kinds of electron-impact studies have been conducted over the years [1–10]. The partial ionization cross section for the production of O^+ has been determined from ion-yield measurements [2–4], and the kinetic-energy (KE) distributions of O^+ have been measured using a time-of-flight technique [5,6] and, more recently, the velocity map imaging method [7]. Multipeaked KE distributions have been observed [5–9], suggesting the presence of four main O^+ groups with peak energies of KE = 0.8, 2, 3, and 5 eV [1], though there is difficulty in deconvoluting individual ionization channels from the data due to the significant overlapping of their contributions [7]. Despite the difficulty, the 0.8 eV peak has unambiguously

been ascribed to predissociation from the $B\,^2\Sigma_g^-$ ion state to the lowest dissociation limit $O^+(^4S) + O(^3P)$. Also studied are the angular distributions of O^+ ions emitted following dissociation. At incident energies close to ionization thresholds, angular anisotropies were observed [6,8–10] and used to identify the symmetry of the O_2^+ states by means of Dunn's rule [11]. On the other hand, at incident energy above ~ 50 eV, the fragment ions were found to be emitted isotopically since the angular anisotropy was mostly smeared out due to summing up contributions from various ionization channels [1,9].

While the partial ionization cross sections and some important insights into the reactions have been provided by those studies, the dynamics of each reaction channel has not been well understood. Since the ion measurements provide no information about the energy transferred from the projectile electron to the target and its partition between O_2^+ and the ejected electron, contributions from different reaction pathways are indistinguishable, making it difficult to unveil the individual dissociative ionization dynamics. It is in sharp contrast to the case for photoinduced dissociative ionization, where deep insights have been obtained into the individual reaction dynamics through studies using various experimental techniques, such as photo-electron photo-ion coincidence (PEPICO) spectroscopy [12–16], threshold PEPICO (TPEPICO) spectroscopy [17–21], and pump and probe photoionization spectroscopy [22].

More detailed information about the electron-induced dissociative ionization can be obtained by imaging velocity distribution of fragment ions in conjunction with electron energy-loss spectroscopy (EELS). Conducting measurements of the energies and momenta of the scattered electron and fragment ions makes it possible to examine how the probability of each dissociative ionization channel depends upon the energy and momentum transferred from the projectile electron to the target. Furthermore, if the molecular ion dissociates much faster than it rotates, the process can be assessed in the molecular-frame since the direction of the fragment-ion

---

[*]Author to whom correspondence should be addressed: noboru.watanabe.e2@tohoku.ac.jp

departure coincides with the molecular orientation at the moment of electron collision [23–27]. Even if the lifetime of the parent ion is not negligibly short compared to the period of molecular rotation, the orientation of the target is still reflected in the angular distribution of the fragment ions, though the effect is somewhat smeared out [12,28], as will be discussed in detail later.

Although scattered electron-fragment-ion coincidence experiments or $(e, e + \text{ion})$ experiments were carried out extensively for molecules, their aims were generally to simulate photo-induced dissociative ionization [29,30]. Thereby, most $(e, e + \text{ion})$ measurements have been performed in the dipole regime, where the momentum transfer is practically zero, and owing to experimental difficulties, only a small number of $(e, e + \text{ion})$ studies have been reported so far for the nondipole regime [31–33], being inaccessible by photo-absorption measurements. Furthermore, the recoil momenta of ions detected in coincidence with electron have not been measured in the $(e, e + \text{ion})$ studies. Under the circumstances, we have recently developed a method to perform electron-ion coincidence experiments over a wide momentum transfer region with measuring the recoil momenta of the ions [34], and applied it to studies on the inner-valence ionization of the nitrogen molecule [35,36]. It has been shown that the technique offers a powerful means to investigate the dissociative ionization dynamics of molecules.

In the present work, we have performed $(e, e + \text{ion})$ experiments on O_2 for advancing our understanding of electron-induced dissociative ionization of the molecule. The electron-ion coincidence data have been collected for the inner-valence ionization of O_2 using an incident electron energy of 1.4 keV. By analyzing the data, partial ion yield spectra have been obtained for transitions to individual ion states, allowing us to investigate state-specific momentum-transfer dependence of the dissociative ionization. Furthermore, angular distributions of fragment ions have been investigated to get insight into the stereodynamics in the electron-O_2 collision processes.

II. EXPERIMENT

In the present work, we used an electron-ion coincidence apparatus developed in our laboratory. Details of the apparatus have been described elsewhere [34]. In short, it consists of an electron gun, an energy-dispersive electron spectrometer, and an ion momentum imaging spectrometer. A continuum electron beam is chopped at 62.5 kHz by applying rectangular voltage pulses to a deflector electrode placed before the exit apertures of the electron gun. The pulsed electron beam is crossed at right angles with the molecular beam effusing from a gas nozzle with 0.5 mm inner diameter. Electrons scattered at a particular angle of θ with respect to the incident beam direction are selected by the entrance apertures of the electron spectrometer and decelerated to ~ 53 eV by means of an electrostatic lens system [37]. The electrons are then dispersed by a hemispherical analyzer and detected by a microchannel plate detector with a delay line anode for position readout (RoentDek, DLD40 [38]).

Triggered by the electron detection, a homogeneous electric field is applied to the interaction region to extract ions into the momentum imaging spectrometer equipped with a time-

and position-sensitive detector (RoentDek, DLD80 [38]). The spectrometer is placed above the interaction region in the vertical direction with respect to the electron scattering plane, which is defined by the momenta of the incident and scattered electrons. The recoil momentum of the ion can be determined from its time of flight (TOF) and arrival positions at the detector. The background due to false coincidences has been estimated from the measurement of ions produced by the incident electron pulse which passes through the interaction region shortly after the detection of an electron. The ions collected in this way are uncorrelated to the detected electron and thus allow us to infer the contribution of false coincidence events.

Electron-ion coincidence experiments for O_2 were carried out at scattering angles of $\theta = 2.2°$, $4.2°$, and $8.2°$. The temporal width of the pulsed electron beam was 170 ns. In the measurements, incident electron energies of 1393, 1398, and 1403 eV were used, which cover energy-loss regions of $E = 19$–30, 24–35, and 29–40 eV, respectively. Electron energy-loss spectra thus obtained were normalized in the overlapping E regions and combined with each other. The energy resolution was estimated to be 0.8 eV full width at half maximum (FWHM) from the peak profile of the elastic scattering. In the measurements, commercially available O_2 gas having 99.99995% minimum stated purity (Taiyo Nippon Sanso Co.) was used without further purification. The experimental result was obtained by accumulating data at an ambient sample gas pressure of 1.0×10^{-4} Pa for $\sim$1–4 weeks runtime at each incident electron energy and scattering angle.

III. THEORY

A. Electron scattering cross section

The double differential cross section of high-energy electron scattering is related to the differential generalized oscillator strength (GOS), df/dE, by the Bethe-Born formula [39,40],

$$\frac{\partial^2 \sigma}{\partial \Omega \partial E} = \frac{|\boldsymbol{k}_1|}{|\boldsymbol{k}_0|} \frac{2}{K^2 E} \frac{df(\boldsymbol{K}, E)}{dE}. \tag{1}$$

Hartree atomic units are used unless noted otherwise. Here, $\boldsymbol{k}_0$ and $\boldsymbol{k}_1$ denote the momenta of the incident and scattered electrons, E is the electron energy loss, and $\boldsymbol{K}$ ($=\boldsymbol{k}_0 - \boldsymbol{k}_1$) is the momentum transferred from the projectile electron to the target. The magnitude of the momentum transfer, $K (=|\boldsymbol{K}|)$, is related to the scattering angle θ as $K = \{k_0^2 + k_1^2 - 2k_0 k_1 \cos \theta\}^{1/2}$. The GOS is expressed as [39,40]

$$\frac{df(\boldsymbol{K}, E)}{dE} = \frac{2E}{K^2} \sum_n \left| \langle \Phi_n | \sum_j \exp(i\boldsymbol{K} \cdot \boldsymbol{r}_j) | \Phi_0 \rangle \right|^2 \delta(E - E_{n0}), \tag{2}$$

where Φ_0 and Φ_n represent the wave functions of the initial and final target states, respectively, E_{n0} is the energy difference between these states, and $\boldsymbol{r}_j$ is the position of the jth electron. The exponential term in Eq. (2) can be expanded into a power series as $\exp(i\boldsymbol{K} \cdot \boldsymbol{r}_j) = 1 + i\boldsymbol{K} \cdot \boldsymbol{r} - (\boldsymbol{K} \cdot \boldsymbol{r})^2/2! - i(\boldsymbol{K} \cdot \boldsymbol{r})^3/3! + \cdots$. In the limit of $K = 0$, contributions from the second- and higher-order terms with respect to K vanish and the GOS converges to the optical oscillator strength

(OOS) [39],

$$\lim_{K \to 0} \frac{df(\boldsymbol{K}, E)}{dE} = 2E \sum_n \left| \langle \Phi_n | \sum_j \hat{\boldsymbol{K}} \cdot \boldsymbol{r}_j | \Phi_0 \rangle \right|^2 \delta(E - E_{n0}),$$

(3)

where $\hat{\boldsymbol{K}} = \boldsymbol{K}/K$. It implies that at $K \sim 0$, electric dipole transitions are dominant and the electron scattering cross section is proportional to the photo-absorption cross section. On the other hand, contributions from electric quadrupole and higher multipole transitions become larger with the increase of K. Hence, measurements at nonzero momentum transfer allow us to investigate dipole-forbidden transitions.

B. Angular distribution of fragment ions

The electron scattering cross section depends upon the orientation of the target molecule at the moment of electron collision. If the molecular ion dissociates much faster than it rotates, the fragment emission direction coincides with the initial molecular orientation. Within this axial-recoil approximation, the stereodynamics in electron-molecule collision processes is directly visible by observing the angular anisotropy appearing in the fragment-ion distribution [11,23]. For analyzing experimental results, we have developed a compact analytical form of the ion angular distribution. A detailed derivation of the analytical form is presented elsewhere [36]. Briefly, the transition matrix of the high-energy electron-impact ionization can be written as

$$T_{n0} = \langle \psi_{\boldsymbol{p}}^{(-)} \Phi_n^{\text{ion}} | \sum_j \exp(i\boldsymbol{K} \cdot \boldsymbol{r}_j) | \Phi_0 \rangle$$
$$= \langle \psi_{\boldsymbol{p}}^{(-)}(\boldsymbol{r}) | \exp(i\boldsymbol{K} \cdot \boldsymbol{r}) | \varphi_n(\boldsymbol{r}) \rangle.$$

(4)

Here, $\psi_{\boldsymbol{p}}^{(-)}$ denotes the wave function of the ejected electron with momentum $\boldsymbol{p}$ and φ_n is the Dyson orbital, which is defined as the overlap between the N-electron neutral state Φ_0 and $(N-1)$-electron ion state Φ_n^{ion}. It is convenient to expand $\psi_{\boldsymbol{p}}^{(-)}$ in terms of spherical harmonics as

$$\psi_{\boldsymbol{p}}^{(-)} = \sum_{l_{ej}, m_{ej}} i^{l_{ej}} e^{-i\delta_{l_{ej}, m_{ej}}} Y_{l_{ej} \, m_{ej}}^*(\hat{\boldsymbol{p}}) R_{p, l_{ej}, m_{ej}}(\boldsymbol{r}),$$

(5)

where $\delta_{l_{ej}, m_{ej}}$ is the phase shift of a partial wave with azimuthal quantum number l_{ej} and magnetic quantum number

m_{ej}. Similarly, an exponential function in Eq. (4), $\exp(i\boldsymbol{K} \cdot \boldsymbol{r})$, is expanded in terms of spherical harmonics $Y_{l0}(\hat{\boldsymbol{r}})$ using a coordinate system with the z axis pointed along the direction of $\boldsymbol{K}$ (laboratory frame). The resultant expression is then transformed to the form in the molecular frame, in which the molecular axis is taken to be the z axis, by means of the Wigner rotation matrix $D_{m_\gamma 0}^l(\hat{\boldsymbol{R}}_\gamma)$ [41],

$$\exp(i\boldsymbol{K} \cdot \boldsymbol{r}) = 4\pi \sum_{l, m_\gamma} i^l j_l(Kr) \sqrt{\frac{2l+1}{4\pi}} Y_{lm_\gamma}(\hat{\boldsymbol{r}}) D_{m_\gamma 0}^l(\hat{\boldsymbol{R}}_\gamma).$$

(6)

Here, $j_l(Kr)$ denotes the spherical Bessel function of order l and $\hat{\boldsymbol{R}}_\gamma$ is the Euler angle specifying the orientation of the molecule. The substitution of Eqs. (5) and (6) into Eq. (4) leads to

$$T_{n0} = \sum_{l, l_{ej}, m_{ej}, m_\gamma} i^{l - l_{ej}} e^{i\delta_{l_{ej}, m_{ej}}} Y_{l_{ej} \, m_{ej}}(\hat{\boldsymbol{p}})$$
$$\times D_{m_\gamma 0}^l(\hat{\boldsymbol{R}}_\gamma) d_{l_{ej}, m_{ej}, l, m_\gamma}(K)$$

(7)

with

$$d_{l_{ej}, \, m_{ej}, \, l, \, m_\gamma}(K)$$
$$= \sqrt{4\pi(2l+1)} \langle R_{p, l_{ej}, m_{ej}} | j_l(Kr) Y_{lm_\gamma}(\hat{\boldsymbol{r}}) | \varphi_n \rangle.$$

(8)

For a linear molecule, the conservation law of angular momentum around the molecular axis requires $m_{ej} = m_\gamma + m_n$, where m_n is the angular momentum quantum number of the Dyson orbital.

Since the ejected electron is not detected in (*e*, *e* + ion) measurements, the obtainable value is the ionization cross section averaged over the direction of $\boldsymbol{p}$. We thus integrate $|T_{n0}|^2$ over the solid angle of the electron emission, and subsequently take the summation over m_n to take into account the degeneracy of the final ion state. As a consequence, the following expression is obtained:

$$\sum_{m_n} \int |T_{n0}|^2 d\hat{\boldsymbol{p}} = \sum_{L_\gamma = 0} b_{L_\gamma} D_{00}^{L_\gamma}(\hat{\boldsymbol{R}}_\gamma)$$

(9)

with

$$b_{L_\gamma} = \sum_{l, l'} \langle l \, 0, l' \, 0 | L_\gamma 0 \rangle \sum_{l_{ej}, m_{ej}, m_n} i^{l - l'} d_{l_{ej}, m_{ej}, l, m_{ej} - m_n} d_{l_{ej}, m_{ej}, l', m_{ej} - m_n}^* (-1)^{m_n - m_{ej}} \langle l \, m_{ej} - m_n, l' - m_{ej} + m_n | L_\gamma \, 0 \rangle.$$

(10)

Since we are now considering a linear molecule, the following relation can be used: $D_{00}^{L_\gamma}(\hat{\boldsymbol{R}}_\gamma) = P_{L_\gamma}(\cos \phi_K)$, where P_{L_γ} is a Legendre polynomial of order L_γ and ϕ_K is the angle of the molecular axis with respect to the momentum

transfer vector $\boldsymbol{K}$. For a homonuclear diatomic molecule such as O_2, the terms with $L_\gamma = $ odd in Eq. (9) vanish due to the reflection symmetry of the molecule, and hence the ion angular distribution for a nonrotating molecule $I^0(\phi_K)$ can be

written as

$$I^0(\phi_K) = C\{1 + \beta_2^0 P_2(\cos\phi_K) + \beta_4^0 P_4(\cos\phi_K) + \cdots\},$$

(11)

where C is a proportional constant and $\beta_i^0 = b_i/b_0$. As discussed in our earlier paper, if K is not significantly large, the magnitude of b_{L_γ} with large L_γ is negligibly small and hence the terms with $L_\gamma \geqslant 6$ are omitted from Eq. (11). Finally, the following compact analytical function is derived for the fragment-ion angular distribution:

$$I^0(\phi_K) \approx C\{1 + \beta_2^0 P_4(\cos\phi_K) + \beta_4^0 P_4(\cos\phi_K)\}. \quad (12)$$

It is worthwhile to consider the form of the ion angular distribution at $K = 0$, where the electron scattering cross section is proportional to the photo-absorption cross section. Under the condition, $I^0(\phi_K)$ becomes equivalent to the photo-ion angular distribution, which is characterized by a single number, the so-called asymmetry parameter β, and can be expressed as $I(\phi) \propto \{1 + \beta P_2(\phi)\}$ with ϕ being the angle made between the photon polarization vector and molecular axis. It follows that

$$\beta_2^0(K)\big|_{K=0} = \beta, \quad (13a)$$

$$\beta_4^0(K)\big|_{K=0} = 0. \quad (13b)$$

$I^0(\phi_K)$ can thus be regarded as an extension of photo-ion angular distribution into a finite momentum transfer regime, and thereby $\beta_2^0(K)$ and $\beta_4^0(K)$ are referred to as generalized asymmetry parameters, which govern the angular anisotropy of fragment-ion emission induced by electron impact.

If the lifetime of the molecular ion τ is not negligibly short compared to the period of molecular rotation, the axial-recoil approximation is not valid and the effects of the rotational motion should be taken into account. Here we use a theory developed by Jonah [28] and Monahan [12] to predict the effects on the $\cos^2\phi_K$ and $\cos^4\phi_K$ terms constituting $P_2(\cos\phi_K)$ and $P_4(\cos\phi_K)$ in Eq. (12). According to the theory, the observable distributions, $\Gamma_2(\phi_K)$ and $\Gamma_4(\phi_K)$, for the initial distributions, $\cos^2\phi_K$ and $\cos^4\phi_K$, are expressed as [12]

$$\Gamma_2(\phi_K) = \frac{1+\alpha^2}{4+\alpha^2}\cos^2\phi_K + \frac{1}{4+\alpha^2}, \quad (14a)$$

$$\Gamma_4(\phi_K) = \frac{(\alpha^4 + 10\alpha^2 + 9)\cos^4\phi_K + 6(\alpha^2+1)\cos^2\phi_K + 9}{(\alpha^2+4)(\alpha^2+16)},$$

(14b)

where $a = (\tau\omega)^{-1}$ with ω being the angular frequency of the molecular rotation. The replacement of $\cos^2\phi_K$ and $\cos^4\phi_K$ by $\Gamma_2(\phi_K)$ and $\Gamma_4(\phi_K)$ changes the Legendre polynomial functions to $\langle P_2(\cos\phi_K)\rangle$ and $\langle P_4(\cos\phi_K)\rangle$:

$$\langle P_2(\cos\phi_K)\rangle = \frac{\alpha^2+1}{\alpha^2+4}P_2(\cos\phi_K), \quad (15a)$$

$$\langle P_4(\cos\phi_K)\rangle = \frac{(\alpha^2+9)(\alpha^2+1)}{(\alpha^2+4)(\alpha^2+16)}P_4(\cos\phi_K). \quad (15b)$$

From the results, it has been deduced that the ion angular distribution for a rotating molecule $I(\phi_K)$ has the same

TABLE I. Vertical ionization potentials (IPs) of O_2 [42].

Ion states	Vertical IP's (eV)	Main electronic configurations
$B\,^2\Sigma_g^-$	20.3	$(3\sigma_g)^{-1}$
$3\,^2\Pi_u$	23.9	$(1\pi_u)^{-1}$
$c\,^4\Sigma_u^-$	24.6	$(2\sigma_u)^{-1}$
$2\,^2\Sigma_u^-$	27.3	$(3\sigma_g)^{-1}(1\pi_u)^{-1}(1\pi_g)^{+1}$ and $(2\sigma_u)^{-1}$
$2\,^4\Sigma_u^-$		$(3\sigma_g)^{-1}(1\pi_u)^{-1}(1\pi_g)^{+1}$ and $(2\sigma_u)^{-1}$
$3\,^2\Sigma_u^-$	33.6	$(3\sigma_g)^{-1}(1\pi_u)^{-1}(1\pi_g)^{+1}$ and $(2\sigma_u)^{-1}$

functional form as Eq. (12),

$$I(\phi_K) \approx C\{1 + \beta_2 P_2(\cos\phi_K) + \beta_4 P_4(\cos\phi_K)\}, \quad (16)$$

while the generalized asymmetry parameters are changed from β_2^0 and β_4^0 for a nonrotating molecule to the observable values, β_2 and β_4:

$$\beta_2 = \frac{\alpha^2+1}{\alpha^2+4}\beta_2^0, \quad (17a)$$

$$\beta_4 = \frac{(\alpha^2+9)(\alpha^2+1)}{(\alpha^2+4)(\alpha^2+16)}\beta_4^0. \quad (17b)$$

At the limit of long lifetime ($\tau = \infty$), $\beta_2 = (1/4)\beta_2^0$ and $\beta_4 = (9/64)\beta_4^0$.

IV. RESULTS AND DISCUSSION

A. Fragment-ion-yield spectra

Molecular oxygen belongs to the $D_{\infty h}$ point group and its ground state has an electronic configuration of $(1\sigma_g)^2(1\sigma_u)^2(2\sigma_g)^2(2\sigma_u)^2(3\sigma_g)^2(1\pi_u)^4(1\pi_g)^2$ [42]. Dissociative ionization in the measured energy-loss region, $E = 19$–40 eV, is mainly due to the removal of an electron from the $3\sigma_g$ and $2\sigma_u$ orbitals [19,42]. As an example of the experimental results, we present an energy correlation diagram for $\theta = 2.2°$ in Fig. 1(a), which was constructed by plotting the number of electron-O^+ coincidence events as a function of electron energy loss and kinetic energy of O^+. Figure 1(b) shows the fragment-ion-yield spectra of O_2 in the form of relative GOS distributions. Vertical bars indicate ionization potentials (IPs) reported in the literature [42]. The spectra were constructed from the electron-O^+ coincidence data measured at $\theta = 2.2°$, $4.2°$, and $8.2°$, which correspond to $K^2 = 0.16$, 0.56, and 2.10 a.u., respectively. The associated OOS distribution [43], which is equivalent to GOS at zero momentum transfer, is also depicted in the figure. All spectra were normalized at $E = 36$ eV for comparison of the spectral shapes. It can be seen that there is a drastic change of the spectrum; the relative intensity of the low-E component rapidly decreases with the increase of K^2, indicating strong momentum transfer dependence of the ionization dynamics.

In the E region under investigation, several dissociative ionization paths are activated. The associated vertical IPs and their assignments are listed in Table I, together with the main electronic configurations of the O_2^+ states [42]. The lowest ionization transition is attributed to the formation of the $B\,^2\Sigma_g^-$ state with a single-hole configuration, $(3\sigma_g)^{-1}$. Photoelectron spectroscopy (PES) has revealed its vertical IP to be 20.3 eV. At IP ~ 23–25 eV, two bands are discernible

TABLE II. Dissociation limits and dissociative energies of O_2^+ [16,19].

Label	Products	Dissociation energy (eV)	Arising O_2^+ states
L_1	$O^+(^4S) + O(^3P)$	18.733	$^{2,4,6}(\Sigma^+, \ \Pi)_{g,u}$
L_2	$O^+(^4S) + O(^1D)$	20.700	$^4(\Sigma^-, \ \Pi, \ \Delta)_{g,u}$
L_3	$O^+(^2D) + O(^3P)$	22.057	$^{2,4}(\Sigma^+(2), \ \Sigma^-, \ \Pi(3), \ \Delta(2), \ \Phi)_{g,u}$
L_4	$O^+(^4S) + O(^1S)$	22.923	$^4\Sigma^-_{g,u}$
L_5	$O^+(^2P) + O(^3P)$	23.750	$^{2,4}(\Sigma^+, \ \Sigma^-(2), \ \Pi(2), \ \Delta)_{g,u}$
L_6	$O^+(^2D) + O(^1D)$	24.024	$^2(\Sigma^+(2), \ \Sigma^-(3), \ \Pi(4), \ \Delta(3), \ \Phi(2), \ \Gamma)_{g,u}$

in the photoelectron spectrum, which have been assigned to the $3\,^2\Pi_u$ and $c\,^4\Sigma_u^-$ states with single-hole configurations $(1\pi_u)^{-1}$ and $(2\sigma_u)^{-1}$, respectively [44]. For higher IP, broad ionization bands appear around 27 and 33 eV [19]. The former is ascribed to ionization to two close-lying states, $2\,^2\Sigma_u^-$ and $2\,^4\Sigma_u^-$, and the latter to the $3\,^2\Sigma_u^-$ ionization. Their main electronic configurations are all mixtures of $(3\sigma_g)^{-1}(1\pi_u)^{-1}(1\pi_g)^{+1}$ and $(2\sigma_u)^{-1}$. The fragment-ion-yield spectra contain contributions from all these ionization transitions and the corresponding continuum bands overlap with each other.

A further analysis was performed to elucidate ionization transitions responsible for the observed momentum transfer dependence. PEPICO studies have revealed that there are

correlations between the O_2^+ states formed and the kinetic-energy (KE) distribution of O^+ [13,16,19]. Thereby, individual ionization transitions can, in principle, be isolated from each other by analyzing the KE of O^+ ions detected in coincidence with scattered electrons. Dissociation limits of O_2^+ [16,19] relevant to the present study are presented in Table II and associated potential-energy curves reported in the literature [19,45,46] are depicted in Fig. 2(a). Figure 2(b) shows the experimental KE distributions of the O^+ fragment for $\theta = 2.2°$, $4.2°$, and $8.2°$ at $E = 19$–30 eV. They all exhibit a maximum around 0.8 eV and a weaker band peaked at ~ 1.9 eV; the latter is followed by a broad tail in the higher-energy side. From results of PEPICO studies, the 0.8 eV band can be attributed to dissociation from the $B\,^2\Sigma_g^-$ state to the first dissociation limit L_1: $O^+(^4S) + O(^3P)$, while the low KE component, $< \sim 0.4$ eV, is caused by the $3\,^2\Pi_u$ state, whose major dissociation channel is decay into the fifth limit, L_5: $O^+(^2P) + O(^3P)$ [13]. In contrast to the $3\,^2\Pi_u$ state, the close-lying $c\,^4\Sigma_u^-$ state primarily dissociates toward lower limits, L_1 and L_2 [$O^+(^4S) + O(^1D)$] [16]. Here the KE of O^+ is ~ 2.9 eV for $c\,^4\Sigma_u^- \to L_1$ and that for $c\,^4\Sigma_u^- \to L_2$ is ~ 1.9 eV. Besides, dissociation from the $2\,^2\Sigma_u^-$ and $2\,^4\Sigma_u^-$ states to L_5 results in the yield of O^+ with KE ~ 2 eV [19], and it can thus be deduced that the 1.9 eV peak of the KE distribution is mostly attributed to the $c\,^4\Sigma_u^-$, $2\,^2\Sigma_u^-$, and $2\,^4\Sigma_u^-$ ionization. It should be noted that the $2\,^2\Sigma_u^-$ and $2\,^4\Sigma_u^-$ states correlate not only to L_5 but also to the

(a) Energy correlation diagram of electron-O^+ coincidence events for $\theta = 2.2°$
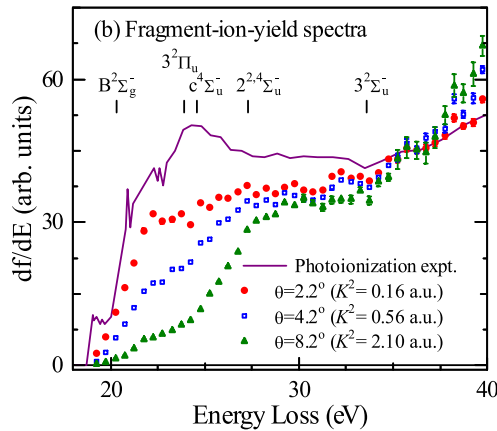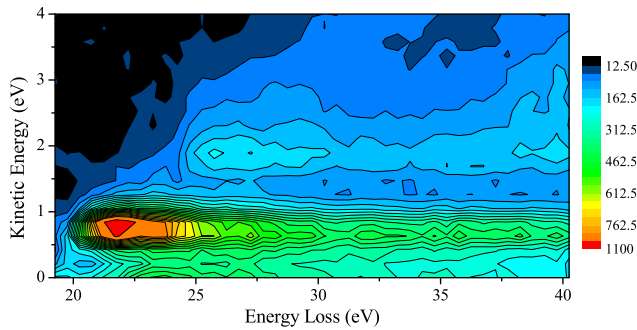

FIG. 1. (a) Electron-energy-loss and kinetic-energy correlation diagram of electron-O^+ coincidence events for $\theta = 2.2°$. (b) Fragment-ion-yield spectra of O_2 constructed from the electron-O^+ coincident data for $\theta = 2.2°$, $4.2°$, and $8.2°$. The solid line represents the result of photoionization experiment [43].
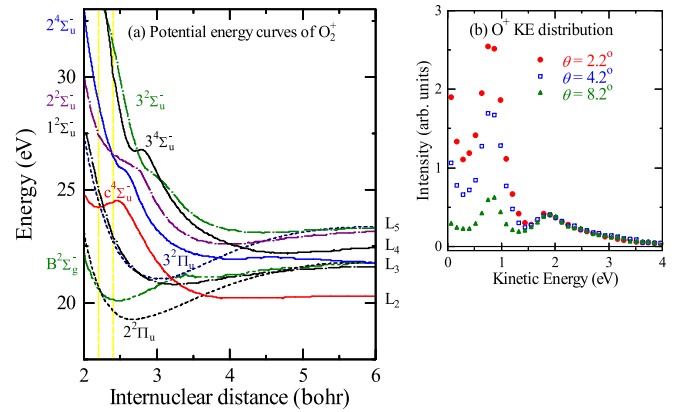
FIG. 2. (a) Potential-energy curves of the electronic states of O_2^+ [19,45,46]. The Franck-Condon region (2.2–2.4 bohr) is denoted by the vertical lines. (b) The kinetic-energy distributions of O^+ constructed from the coincidence data at $E = 19$–30 eV. For ease of comparison, the distributions are scaled so that their intensities coincide with each other at KE = 1.9 eV.
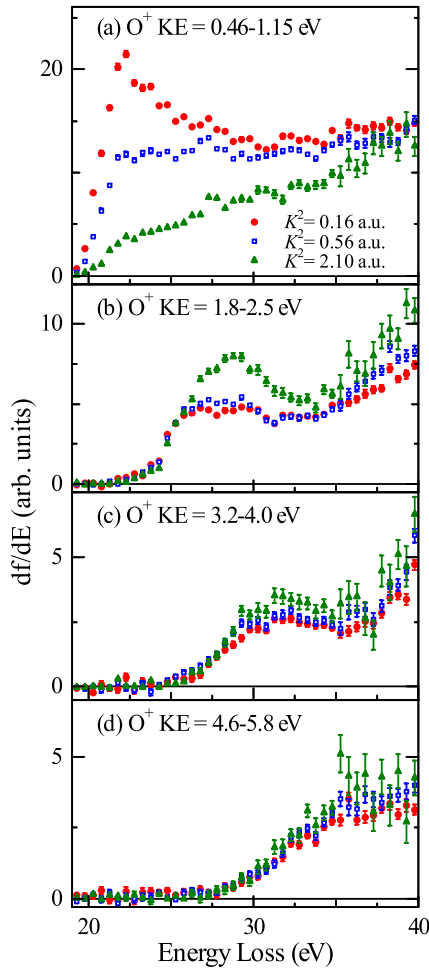
FIG. 3. Fragment-ion-yield spectra constructed from the coincidence data with detection of O^+ having KE = (a) 0.46–1.15, (b) 1.8–2.5, (c) 3.2–4.0, and (d) 4.6–5.8 eV, which are mainly associated with ionization to the $B\,^2\Sigma_g^-$, $\{c\,^4\Sigma_u^- + 2\,^2\Sigma_u^- + 2\,^4\Sigma_u^-\}$, $\{2\,^2\Sigma_u^- + 2\,^4\Sigma_u^-\}$, and $3\,^2\Sigma_u^-$ states, respectively. See text for details.

third dissociation limit, L_3: $O^+(^2D) + O(^3P)$, and O^+ ions with KE ~ 3 eV are released through the $2\,^2\Sigma_u^- \rightarrow L_3$ and $2\,^4\Sigma_u^- \rightarrow L_3$ paths. The major dissociation channels of the remaining $3\,^2\Sigma_u^-$ state are $3\,^2\Sigma_u^- \rightarrow L_5$ and $3\,^2\Sigma_u^- \rightarrow L_6$, which cause the ejection of O^+ with KE ~ 5 eV [19]. Based on the above argument, we have separated contributions from different ionization channels by selecting coincidence events with detection of O^+ having KE = 0.46–1.15, 1.8–2.5, 3.2–4.0, and 4.6–5.8 eV, respectively. These KE regions can be mainly associated with the $B\,^2\Sigma_g^-$, $\{c\,^4\Sigma_u^- + 2\,^2\Sigma_u^- + 2\,^4\Sigma_u^-\}$, $\{2\,^2\Sigma_u^- + 2\,^4\Sigma_u^-\}$, and $3\,^2\Sigma_u^-$ ionization transitions, respectively. The fragment-ion-yield spectra thus obtained for each KE region are depicted in Figs. 3(a)–3(d).

It is evident from Fig. 3(a) that the spectra for the $B\,^2\Sigma_g^-$ ionization show a drastic change upon varying K^2. For the smallest K^2, a broad maximum is observed at $E \sim 22$ eV, while it disappears in the spectra for $K^2 = 0.56$ and 2.10 a.u. Photoionization studies have shown the presence of a σ_u shape resonance in the $B\,^2\Sigma_g^-$ channel [45], which is described as temporal trapping of the ejected electron by the molecular potential barrier. The effect has been observed as a significant

enhancement of the photoionization cross section at $h\nu \sim 23$ eV. Such a phenomenon may also take place in electron-impact ionization and the broad peak structure observed at $K^2 = 0.16$ a.u. can be ascribed to the shape-resonance effect. Also seen from Fig. 3(a) is that the relative intensity around the peak position quickly falls down with the increase of K^2. In contrast to the dominance of dipole transitions at $K^2 \sim 0$, contributions from quadrupole and higher multipole transitions become larger at higher K^2. The result therefore indicates that the influence of nondipole interactions strongly suppresses the σ_u shape resonance in the $B\,^2\Sigma_g^-$ ionization. A similar tendency has also been observed for the σ_u shape resonance in the $F\,^2\Sigma_g^+$ ionization of N_2 [36]. It is likely that the ionization cross section for the shape-resonance region sensitively reflects the shape of the wave function of the electron trapped within the potential barrier and exhibits significant momentum-transfer dependence, similar to cases of transitions to discrete bound states, where rapid changes of GOSs with K^2 have generally been observed [40,47].

The momentum-transfer dependence of the spectra for the $\{c\,^4\Sigma_u^- + 2\,^2\Sigma_u^- + 2\,^4\Sigma_u^-\}$ ionization is considerably different from that of the $B\,^2\Sigma_g^-$ spectra. As can be seen from Fig. 3(b), the spectra for $K^2 = 0.16$ and 0.56 a.u. almost coincide in shape with each other, while for the largest K^2, a broad peak structure shows up at $E \sim 28$ eV. The 28 eV band was first found by a conventional EELS experiment at large momentum transfer and assigned to single-electron excitation from the $2\sigma_g$ orbital to the $1\pi_g$ orbital [48]. Excitation between gerade states is dipole forbidden and is practically inaccessible by EELS measurements at small momentum-transfer and photoabsorption experiments. The highly excited O_2 molecule that is formed may immediately dissociate after Auger decay via the $(2\sigma_u)^{-1}$ or $(3\sigma_g)^{-1}(1\pi_u)^{-1}(1\pi_g)^{+1}$ ion state, and as a consequence the corresponding autoionization band is observed as the broad peak at ~ 28 eV in the fragment-ion-yield spectrum for large K^2, where quadrupole transitions become allowed.

As can be seen from Figs. 3(c) and 3(d), only small changes with K^2 have been observed in the $\{2\,^2\Sigma_u^- + 2\,^4\Sigma_u^-\}$ and $3\,^2\Sigma_u^-$ spectra. One may notice that $(2\sigma_u)^{-1}$ is a main electronic configuration of these three states and also of the $c\,^4\Sigma_u^-$ state, while $(3\sigma_g)^{-1}$ is that of the $B\,^2\Sigma_g^-$ state. The spectra for transitions to O_2^+ states with the $(2\sigma_u)^{-1}$ manifold appear to vary more slowly with K^2, except the $2\sigma_g \rightarrow 1\pi_g$ autoionization band at $E \sim 28$ eV, compared to those for transitions to ion states with the $(3\sigma_g)^{-1}$ manifold. It has been shown that individual ionization transitions depend upon K in different ways, and the $(e, e + \text{ion})$ method offers an opportunity to investigate the state-specific K dependence of electron-induced dissociative ionization.

B. O^+ angular distribution for the $B\,^2\Sigma_g^-$ ionization

We subsequently examine the emission angle of the fragment ion. Figure 4 shows the angular distributions of O^+ generated from the $B\,^2\Sigma_g^-$ state, which were constructed from the electron-ion coincidence data with the detection of O^+ having KE = 0.46–1.15 eV. The number of the coincidence events were plotted as a function of the angle made between the recoil direction of O^+ and the momentum transfer
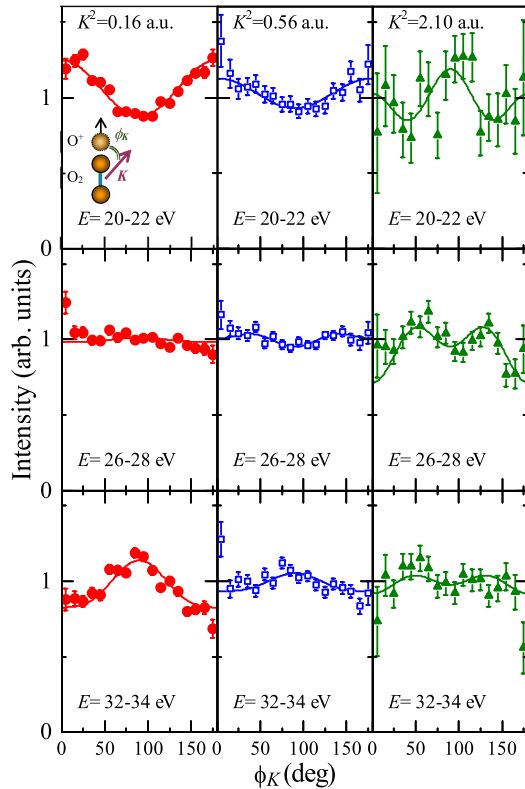
FIG. 4. Angular distributions of O^+ having KE = 0.46–1.15 eV, which are dominantly attributed to dissociation from the $B\,^2\Sigma_g^-$ state to the dissociation limit L_1: $O^+(^4S) + O(^3P)$. Solid lines represent the analytical function $I(\phi_K) = C\{1 + \beta_2 P_2(\cos\phi_K) + \beta_4 P_4(\cos\phi_K)\}$ fitted to experiment. For comparison in shape, all results are scaled so that the proportional coefficient C is equal to 1. See text for details.

FIG. 5. Generalized asymmetry parameters, (a) β_2 and (b) β_4, for the $B\,^2\Sigma_g^-$ ionization at $K^2 = 0.16$, 0.56, and 2.10 a.u. Dashed lines are drawn as a guide for the eye.

vector, ϕ_K. To reproduce the experimental results, the analytic form described in Sec. III, $I(\phi_K) = C\{1 + \beta_2 P_2(\cos\phi_K) + \beta_4 P_4(\cos\phi_K)\}$, was used as a fitting function with C, β_2, and β_4 being treated as fitting parameters. The curves thus obtained are shown as solid lines in the figures. For ease of comparison, all results are scaled so that the proportional coefficient C becomes equal to 1.

It can be seen from Fig. 4 that the anisotropies of the angular distributions are rather small. The $B\,^2\Sigma_g^-$ ion state is predissociative and its lifetime lies in the 0.45–1.5 ps range, depending upon the vibrational level of the ion state. By using the rotational constant of $B = 1.26\,\text{cm}^{-1}$ and by assuming a Maxwell-Boltzmann distribution, Hikosaka *et al.* [49] estimated the mean rotational period of the molecular ion to be $\sim$0.8 ps at 300 K, which is comparable to the predissociation lifetime. The molecular rotation thus leads to considerable reduction of the angular anisotropy of the ion emission.

The generalized asymmetry parameters are used to quantitatively assess the shapes of the angular distributions. β_2 and β_4 are depicted against E in Fig. 5. For $K^2 = 0.16$ a.u., the values of β_4 are zero within the error bars, as expected for small K^2, and the angular anisotropy is practically governed by the $\beta_2 P_2(\cos\phi_K)$ term. From photoionization experiments, the asymmetry parameter β, which coincides with β_2 at $K =$
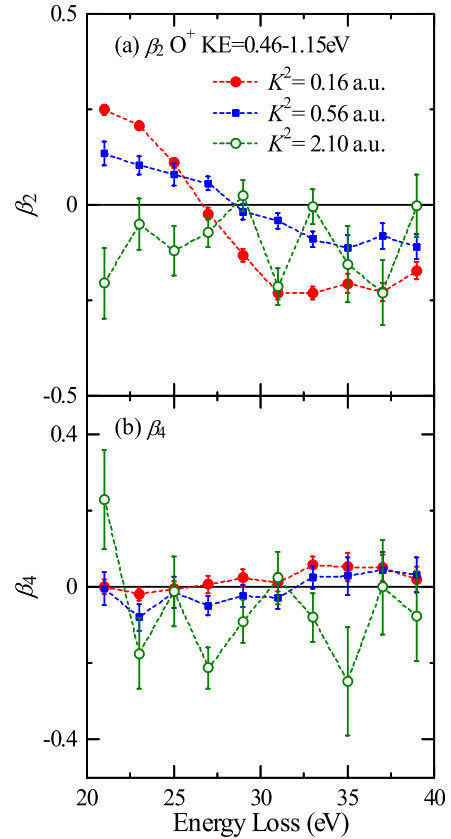
0, was derived for the $B\,^2\Sigma_g^-$ ionization [14,50]. The β values reported in the literature are $\sim$0.3–0.4 near the ionization threshold, 20–21 eV, which appear to be slightly higher than the β_2 value of 0.25 obtained for $K^2 = 0.16$ a.u. at $E = 21$ eV. The difference between the β_2 and β values may be, at least partly, due to the quick suppression of the σ_u shape resonance with the increase of K^2. As can be seen from Fig. 5(a), the value of β_2 monotonically decreases with E and becomes negative above 27 eV. A similar tendency is observed also for $K^2 = 0.56$ a.u., while the absolute value of β_2 becomes smaller due to larger contributions from nondipole transitions. The results indicate that at small K^2, the O^+ ion is preferentially emitted perpendicular to the momentum transfer vector above $\sim$27 eV. The observed behavior is qualitatively consistent with the theoretical prediction of β made by Lin and Lucchese [45], though the measured magnitude of β_2 is much smaller than the theoretical β, caused by the influences of molecular rotation as well as finite momentum-transfer value. The theoretical calculation has shown that β has a large positive value near the ionization threshold due to the σ_u shape-resonance effect, while it has a negative value at high $h\nu$ caused by the dominant π_u component of the ejected electron [45].

For $K^2 = 2.10$ a.u., β_4 is no longer negligibly small and considerably affects the angular anisotropy. It can be seen from Fig. 5 that β_2 and β_4 for $K^2 = 2.10$ a.u. appear to exhibit interesting oscillatory behavior. The origin of the E
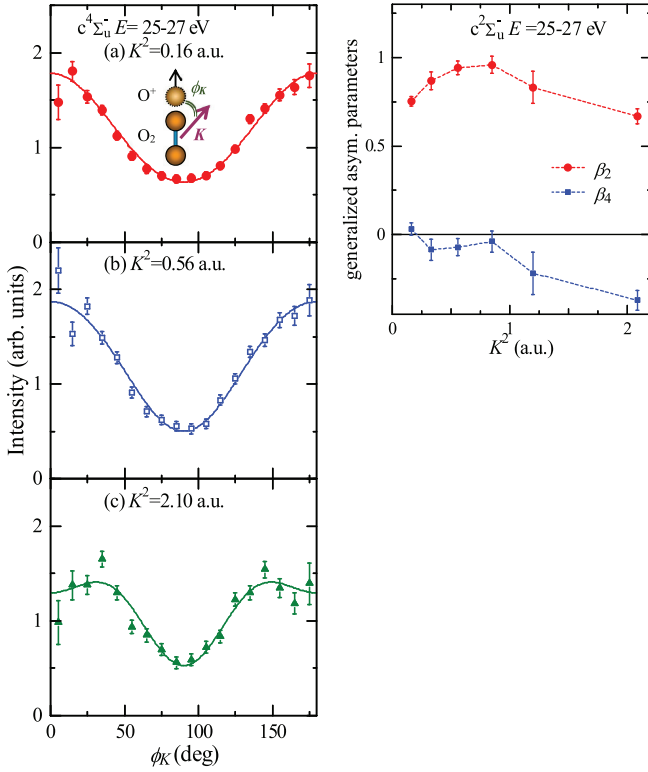
FIG. 6. Left-hand panel: Angular distributions of O^+ having KE = 1.8–2.5 eV at $E = 25$–27 eV, which are mainly associated with the $c^4\Sigma_u^-$ ionization, for $K^2 =$ (a) 0.16, (b) 0.56, and (c) 2.10 a.u. Solid lines represent the analytical function $I(\phi_K) = C\{1 + \beta_2 P_2(\cos \phi_K) + \beta_4 P_4(\cos \phi_K)\}$ fitted to the experiment. For comparison in shape, all results are scaled so that the proportional coefficient C is equal to 1. The right-hand panel depicts $\beta_2(K)$ and $\beta_4(K)$ against K^2, which were obtained by fitting $I(\phi_K)$ to the experimental angular distributions. Dashed lines are drawn as a guide for the eye.

dependence is not clear now, but it may bring insights into the stereodynamics of electron-impact ionization in the nondipole regime.

C. O^+ angular distribution for the $\{c^4\Sigma_u^- + 2^2\Sigma_u^- + 2^4\Sigma_u^-\}$ ionization

We now move our attention to the angular distribution of O^+ ions having KE $\sim$ 1.8–2.5 eV, the ions of which are mostly generated via the dissociation channels of $c^4\Sigma_u^- \to L_2$, $2^2\Sigma_u^- \to L_5$, and $2^4\Sigma_u^- \to L_5$. In particular, the data below $E = 27$ eV can be attributed solely to $c^4\Sigma_u^- \to L_2$, as the IPs for the other two channels, $\sim$27.3 eV, are higher than the energy. First, we focus on the ion angular distributions for $E \sim 25$–27 eV, at which the $c^4\Sigma_u^-$ channel is dominant, and subsequently discuss the results for $E > 27$ eV.

The O^+ angular distributions for the $c^4\Sigma_u^-$ ionization is presented in the left-hand panel of Fig. 6. The $c^4\Sigma_u^-$ ion state is predissociative and its $v = 0$ and 1 vibrational levels are observed in the photoelectron spectrum as sharp peaks at IP = 24.6 and 24.8 eV, respectively [16,20,44]. Contributions from the two vibrational levels cannot be distinguished in the $(e, e + \text{ion})$ measurements and both are included in the angular distributions. It can be seen from the figure that

the $c^4\Sigma_u^-$ ionization preferentially occurs for the molecule having the axis parallel to K at $K^2 = 0.16$ and 0.56 a.u., while the relative intensity around $\phi_K = 0°$ and 180° appreciably decreases at $K^2 = 2.10$ a.u.

Also seen from the figure is that the experimental results have been satisfactorily reproduced by the fitting curves, indicating that the ion angular anisotropy is practically governed by the two parameters, β_2 and β_4. For a quantitative analysis of the K-dependent angular anisotropy, the variations of the parameters with K^2 are depicted in Fig. 6. β_2 and β_4 were determined by fitting $I(\phi_K)$ to the experimental results presented in the figure as well as those obtained from additional measurements at $\theta = 3.2°$, 5.2°, and 6.2° using an incident electron energy of 1393 eV.

It should be noted that the values of β_2 and β_4 are affected by the predissociation lifetimes of the vibrational levels and the branching ratios of relevant dissociative channels. PEPICO studies have revealed that the $v = 1$ level dissociates exclusively toward the second dissociation limit L_2 via tunnelling through the potential barrier [16]. Its predissociation lifetime $\tau_{v=1}$ was measured to be $\sim$0.069 ps [20,51], which is rather short compared to the rotational period of the molecule. On the other hand, the $v = 0$ level, which proceeds mainly to L_1 and L_2, has a much longer lifetime in the range of $\tau_{v=0} \sim 10^{-12}$–10^{-11} s [20], allowing for considerable rotation of O_2^+ prior to dissociation. The influences of the finite lifetimes diminish the β_2 and β_4 values from those for the nonrotating molecule, β_2^0 and β_4^0. It follows from Eq. (17a) that

$$\beta_2 = \beta_2^0\{[(\tau_{v=1}\omega)^2 + 1]/[4(\tau_{v=1}\omega)^2 + 1] + (\sigma_{v=0}/\sigma_{v=1})R_{L2}[(\tau_{v=0}\omega)^2 + 1]/[4(\tau_{v=0}\omega)^2 + 1]\} /\{1 + (\sigma_{v=0}/\sigma_{v=1})R_{L2}\}.$$

Here, $\sigma_{v=0}$ and $\sigma_{v=1}$ indicate the ionization cross sections of the transitions to the $v = 0$ and 1 levels, respectively, and R_{L2} is the branching ratio of the dissociation channel of $c^4\Sigma_u^-(v = 0) \to L_2$. The cross-section ratio $\sigma_{v=0}/\sigma_{v=1}$ can be estimated to be $\sim$2.1 from the intensities of the $v = 0$ and 1 peaks in the photoelectron spectrum [20], and R_{L2} was determined to be 54% using the PEPICO technique [16]. By using values of $\tau_{v=1} = 0.069$ ps, $\tau_{v=0} = 12$ ps [52], and $\omega = 2\pi/0.8$ ps^{-1}, a relation, $\beta_2 = 0.41\beta_2^0$, is obtained from the above equation. Similarly, β_4 may be approximated to $\beta_4 = 0.25\beta_4^0$.

At the limit of $K^2 = 0$, β_2 coincides with the photo-ion asymmetry parameter β. The O^+ photo-ion angular distribution has been investigated so far for the $c^4\Sigma_u^-$ channel both experimentally and theoretically. Here we compare the β_2 value determined for $K^2 = 0.16$ a.u. with the β values reported in the literature. As can be seen from Fig. 6(a), the angular distribution for $K^2 = 0.16$ a.u. is highly anisotropic. The β_2 value of 0.75 ± 0.03 obtained from the data is in reasonable accordance with the experimental β value of 0.55 determined recently by Holland and Shaw for $h\upsilon = 26.0$ eV [50], while it is substantially larger than the value of 0.1 ± 0.05 at $h\upsilon = 27.35$ eV earlier reported by Lafosse *et al.* [14]. It has been pointed out by Lafosse *et al.* that underestimation of their apparatus function may cause the low value of β. The influence of the molecular rotation, which can be roughly
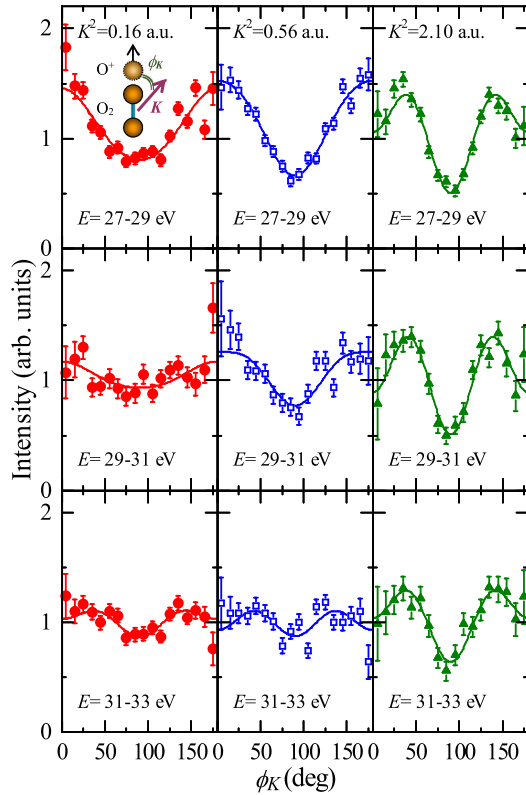
FIG. 7. Angular distributions of O$^+$ having KE $= 1.8$–2.5 eV, which are mainly associated with the $\{c\,^4\Sigma_u^- + 2\,^2\Sigma_u^- + 2\,^4\Sigma_u^-\}$ ionization, at $E = 27$–29, 29–31, and 31–33 eV. Solid lines represent the analytical function $I(\phi_K) = C\{1 + \beta_2 P_2(\cos\phi_K) + \beta_4 P_4(\cos\phi_K)\}$ fitted to the experiment. For comparison in shape, all results are scaled so that the proportional coefficient C is equal to 1.

FIG. 8. Generalized asymmetry parameters (a) β_2 and (b) β_4, for the $\{c\,^4\Sigma_u^- + 2\,^2\Sigma_u^- + 2\,^4\Sigma_u^-\}$ ionization at $K^2 = 0.16$, 0.56, and 2.10 a.u. Dashed lines are drawn as a guide for the eye.

taken into account by multiplying a factor of 0.41 as discussed above, reduces the theoretical value reported by Lin and Lucchese [45] from ~ 1.6 to 0.66, which is in good agreement with the present result. The angular anisotropy observed for $K^2 = 0.16$ a.u. is thus consistent with the result of the recent photoionization study and the theoretical prediction, indicating that the electron-induced $c\,^4\Sigma_u^-$ ionization is mainly governed by dipole interaction at the momentum-transfer value.

We subsequently discuss the momentum-transfer dependences of $\beta_2(K)$ and $\beta_4(K)$. It can be seen from the right-hand panel of Fig. 6 that β_2 increases with K^2 and has a maximum around $K^2 = 0.8$ a.u., while the β_4 values are almost zero at $K^2 < 1$ a.u. Above ~ 1 a.u., the value of β_2 falls down with K^2, while β_4 has an appreciable negative value, leading to the reduction of the relative intensity along the momentum-transfer direction, $\phi_K = 0°$ and $180°$. To our knowledge, there is no available theoretical calculation for these parameters. Since contributions from not only electric dipole but also higher multipole transitions are involved, the generalized asymmetry parameters may provide a test of theoretical calculations for electron-induced inner-valence ionization.

Above 27 eV, not only the $c\,^4\Sigma_u^-$ ionization but also the $2\,^2\Sigma_u^-$ and $2\,^4\Sigma_u^-$ ionization may contribute to the electron-ion coincidence events involving detection of O$^+$ with KE $\sim$
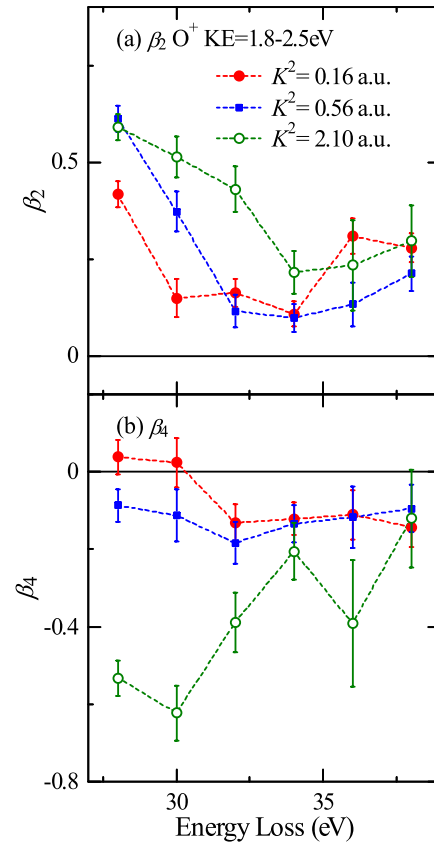
1.8–2.5 eV. Figure 7 shows the ion angular distributions for $E \sim 27$–29, 29–31, and 31–33 eV. The values of β_2 and β_4 are presented as functions of E in Fig. 8. It can be seen from Fig. 7 that O$^+$ is preferentially emitted along the direction parallel to the momentum-transfer vector at $E = 27$–29 eV and $K^2 = 0.16$ and 0.56 a.u. The high values of β_2 are mainly responsible for the observed anisotropy of the angular distributions. On the other hand, β_4 is close to zero for $K^2 = 0.16$ and 0.56 a.u. at the E region and the $\beta_4 P_4(\cos\phi_K)$ term thus has little influence on the angular anisotropy. At higher E, the ion angular distributions become less anisotropic due to the decrease of β_2. The theoretical calculation of the photo-ion asymmetry parameter for the $c\,^4\Sigma_u^-$ and $2\,^2\Sigma_u^-$ ionization [45] predicts that the β values monotonically decrease with E and the tendency is consistent with the experimental result at small K^2, where dipole transitions would be dominant. In contrast to the results for $K^2 = 0.16$ and 0.56 a.u., the angular distribution for $K^2 = 2.10$ a.u. exhibits minima rather than maxima at $\phi_K = 0°$ and $180°$ and it has a double-peaked shape below $E \sim 33$ eV. The double-peaked structure is pronounced at $E \sim 27$–31 eV, around which the $2\sigma_g \rightarrow 1\pi_g$ autoionization band is observed, and it thus can be attributed to the single-electron excitation to the $1\pi_g$ orbital.

To get a qualitative understanding of the result for the autoionization, we examine the transition matrix of the $2\sigma_g \rightarrow 1\pi_g$ excitation within the framework of a single-electron model, $\langle 2\sigma_g| \exp(i\boldsymbol{K} \cdot \boldsymbol{r})|1\pi_g\rangle$. The $2\sigma_g \rightarrow 1\pi_g$ orbitals are
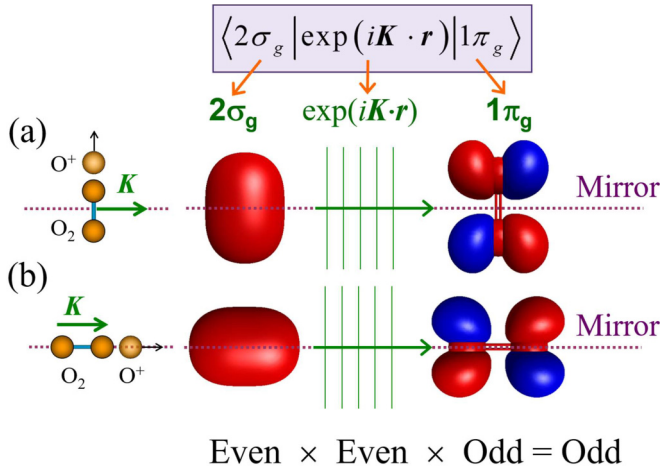
FIG. 9. Schematic representations of the $2\sigma_g \rightarrow 1\pi_g$ excitation when the momentum-transfer vector is (a) perpendicular and (b) parallel to the molecular axis. For both cases, reflection in a mirror plane depicted by a dashed line changes the sign of the $1\pi_g$ orbital, while the symmetry operation leaves the $2\sigma_g$ orbital and the exponential term $\exp(i\mathbf{K} \cdot \mathbf{r})$ unchanged. The integrand in the transition matrix $\langle 2\sigma_g| \exp(i\mathbf{K} \cdot \mathbf{r})|1\pi_g\rangle$ is therefore odd under the reflection operations and the scattering cross section vanishes at $\phi_K = 0°$, $90°$, and $180°$.

depicted in Fig. 9. The $2\sigma_g$ orbital is totally symmetric under all symmetry operations of the $D_{\infty h}$ point group and its shape is rather isotropic. On the other hand, the $1\pi_g$ orbital has an anisotropic shape with a nodal plane perpendicular to the molecular axis. As can be seen from Fig. 9(a), the reflection in the nodal plane changes the sign of the $1\pi_g$ orbital, while the symmetry operation leaves the exponential term $\exp(i\mathbf{K} \cdot \mathbf{r})$ unchanged when $\mathbf{K}$ is perpendicular to the molecular axis. The integrand in the transition matrix is therefore odd under the reflection, and it follows that the scattering cross section vanishes at $\phi_K = 90°$. From a similar consideration for another nodal plane of the $1\pi_g$ orbital through two O atoms, which is depicted in Fig. 9(b), it can be deduced that the transition probability becomes zero at $\phi_K = 0°$. It has been revealed that the observed minima at $\phi_K = 0°$, $90°$, and $180°$ reflect the nodal structure of the $1\pi_g$ orbital. Finite intensities at the minimum positions may be due to the underlying direct ionization continuum at $E \sim 27$–$31\,\text{eV}$. It has been shown that the $(e, e + \text{ion})$ cross section for the autoionization band exhibits a characteristic angular distribution reflecting the anisotropic shape of the molecular orbital to which the target electron is excited.

V. SUMMARY

In this study, we have carried out $(e, e + \text{ion})$ experiments for the inner-valence ionization of O_2. Vector correlations between the linear momenta of the scattered electrons and fragment ions have been measured for $K^2 = 0.16$, 0.56, and 2.10 a.u. using an incident electron energy of 1.4 keV. Fragment-ion-yield spectra have been derived for the $B\,^2\Sigma_g^-$, $\{c\,^4\Sigma_u^- + 2\,^2\Sigma_u^- + 2\,^4\Sigma_u^-\}$, $\{2\,^2\Sigma_u^- + 2\,^4\Sigma_u^-\}$, and $3\,^2\Sigma_u^-$ ionization channels, showing that the individual ionization transitions depend upon K^2 in different ways. In particular, strong momentum-transfer dependence has been observed for the $B\,^2\Sigma_g^-$ ionization due to the rapid suppression of the shape-resonance feature with the increase of K^2.

The angular distributions of O^+ have been examined for the $B\,^2\Sigma_g^-$ and $\{c\,^4\Sigma_u^- + 2\,^2\Sigma_u^- + 2\,^4\Sigma_u^-\}$ ionization. The results are well reproduced by the analytical function, $I(\phi_K) = C\{1 + \beta_2 P_2(\cos\phi_K) + \beta_4 P_4(\cos\phi_K)\}$, indicating that the angular anisotropy of the O^+ emission is practically determined by the two parameters, β_2 and β_4, under the experimental conditions used. For $K^2 = 0.16$ and 0.56 a.u., β_4 is close to zero and the $\beta_2 P_2(\cos\phi_K)$ term has a dominant influence on the angular distribution. In particular for $K^2 = 0.16$ a.u., the values of β_2 have generally been in reasonable agreement with those of the photo-ion asymmetry parameter β due to the dominance of dipole ionization. The experimental results have shown that the angular distributions vary with K^2 and, furthermore, the contribution of the $\beta_4 P_4(\cos\phi_K)$ term becomes appreciable at $K^2 = 2.10$ a.u. The momentum-transfer dependence of β_2 and β_4 may bring information about the stereodynamics of electron-O_2 collision processes in a nondipole regime.

The $2\sigma_g \rightarrow 1\pi_g$ excitation has been observed as a broad peak in the fragment-ion-yield spectrum for the $\{c\,^4\Sigma_u^- + 2\,^2\Sigma_u^- + 2\,^4\Sigma_u^-\}$ ionization, indicating that the highly excited O_2 molecule that is formed may dissociate after Auger decay through the $(2\sigma_u)^{-1}$ or $(3\sigma_g)^{-1}(1\pi_u)^{-1}(1\pi_g)^{+1}$ ion state. The O^+ angular distribution for the $2\sigma_g \rightarrow 1\pi_g$ autoionization band exhibits a double-peaked shape, reflecting the nodal structure of the $1\pi_g$ orbital. It strongly suggests that the $(e, e + \text{ion})$ technique provides a tool to investigate spatial shapes of unoccupied molecular orbitals.

[1] J. W. McConkey, C. P. Malone, P. V. Johnson, C. Winstead, V. McKoy, and I. Kanik, Phys. Rep. **466**, 1 (2008), and references therein.

[2] A. Zecca, G. P. Karwasz, and R. S. Brusa, Riv. Nuovo Cimento **19**, 1 (1996), and references therein.

[3] E. Krishnakumar and S. K. Srivastava, Int. J. Mass Spectrom. Ion Proc. **113**, 1 (1992).

[4] H. C. Straub, P. Renault, B. G. Lindsay, K. A. Smith, and R. F. Stebbings, Phys. Rev. A **54**, 2146 (1996).

[5] B. Van Zyl and T. M. Stephen, Phys. Rev. A **50**, 3164 (1994).

[6] J. A. D. Stockdale and L. Deleanu, Chem. Phys. Lett. **22**, 204 (1973).

[7] J. N. Bull, J. W. L. Lee, and C. Vallance, Phys. Rev. A **91**, 022704 (2015).

[8] A. Matsuo, K. Furuya, and T. Ogawa, Chem. Phys. Lett. **287**, 653 (1998).

[9] R. J. Van Brunt, G. M. Lawrence, L. J. Kieffer, and J. M. Slater, J. Chem. Phys. **61**, 2032 (1974).

[10] A. I. Zhukov, A. N. Zavilopulo, A. V. Snegursky, and O. B. Shpenik, J. Phys. B: At. Mol. Opt. Phys. **23**, 2373S (1990).

[11] G. H. Dunn, Phys. Rev. Lett. **8**, 62 (1962).

[12] J. H. D. Eland and E. J. Duerr, Chem. Phys. **229**, 1 (1998).

[13] A. Lafosse, J. C. Brenot, A. V. Golovin, P. M. Guyon, K. Hoejrup, J. C. Houver, M. Lebech, and D. Dowek, J. Chem. Phys. **114**, 6605 (2001).

[14] A. Lafosse, J. C. Brenot, P. M. Guyon, J. C. Houver, A. V. Golovin, M. Lebech, D. Dowek, P. Lin, and R. R. Lucchese, J. Chem. Phys. **117**, 8368 (2002).

[15] D. Dowek, M. Lebecha, J. C. Houver, and R. R. Lucchese, J. Electron Spectrosc. Relat. Phenom. **141**, 211 (2004).

[16] X. Tang, G. A. Garcia, and L. Nahon, J. Chem. Phys. **148**, 124309 (2018).

[17] M. Richard-Viard, O. Dutuit, M. Lavollée, T. Govers, P. M. Guyon, and J. Durup, J. Chem. Phys. **82**, 4054 (1985).

[18] K. Ellis, R. I. Hall, L. Avaldi, G. Dawber, A. McConkey, L. Andric, and G. C. King, J. Phys. B: At. Mol. Opt. Phys. **27**, 3415 (1994).

[19] Y. Hikosaka, T. Aoto, R. I. Hall, K. Ito, R. Hirayama, N. Yamamoto, and E. Miyoshi, J. Chem. Phys. **119**, 7693 (2003).

[20] A. Padmanabhan, M. A. MacDonald, C. H. Ryan, L. Zuin, and T. J. Reddish, J. Phys. B: At. Mol. Opt. Phys. **43**, 165204 (2010).

[21] X. Tang, X. Zhou, M. Niu, S. Liu, and L. Sheng, J. Phys. Chem. A **115**, 6339 (2011).

[22] W. Siu, F. Kelkensberg, G. Gademann, A. Rouzée, P. Johnsson, D. Dowek, M. Lucchini, F. Calegari, U. De Giovannini, A. Rubio, R. R. Lucchese, H. Kono, F. Lépine, and M. J. J. Vrakking, Phys. Rev. A **84**, 063412 (2011).

[23] R. N. Zare, J. Chem. Phys. **47**, 204 (1967).

[24] M. Takahashi, N. Watanabe, Y. Khajuria, K. Nakayama, Y. Udagawa and J. H. D. Eland, J. Electron Spectrosc. Relat. Phen. **141**, 83 (2004).

[25] M. Takahashi, N. Watanabe, Y. Khajuria, Y. Udagawa, and J. H. D. Eland, Phys. Rev. Lett. **94**, 213202 (2005).

[26] S. Bellm, J. Lower, E. Weigold, and D. W. Mueller, Phys. Rev. Lett. **104**, 023202 (2010).

[27] A. Senftleben, T. Pflüger, X. Ren, O. Al-Hagan, B. Najjari, D. Madison, A. Dorn, and J. Ullrich, J. Phys. B: At. Mol. Opt. Phys **43**, 081002 (2010).

[28] C. Jonah, J. Chem. Phys. **55**, 1915 (1971).

[29] J. W. Gallagher, C. E. Brion, J. A. R. Samson, and P. W. Langhoff, J. Phys. Chem. Ref. Data **17**, 9 (1988), and references therein.

[30] C. E. Brion, K. H. Tan, M. J. van der Wiel, Ph. E. van der Leeuw, J. Electron Spectrosc. Relat. Phen. **17**, 101 (1979).

[31] G. Cooper, J. Stewart-Ornstein, and A. P. Hitchcock, J. Electron Spectrosc. Relat. Phenom. **156-158**, 86 (2007).

[32] K. Yamamoto and Y. Sakai, J. Phys. B: At. Mol. Opt. Phys. **45**, 055201 (2012).

[33] M. Lin, Y.-W. Liu, Z.-P. Zhong, and L.-F. Zhu, Chin. Phys. B **22**, 023404 (2013).

[34] N. Watanabe, T. Hirayama, S. Yamada, and M. Takahashi, Rev. Sci. Instrum. **89**, 043105 (2018).

[35] N. Watanabe, S. Yamada, and M. Takahashi, Phys. Rev. A **95**, 060702(R) (2017).

[36] N. Watanabe, S. Yamada, and M. Takahashi, Phys. Chem. Chem. Phys. **20**, 1063 (2018).

[37] M. Takahashi, N. Watanabe, Y. Wada, S. Tsuchizawa, T. Hirosue, H. Hayashi, and Y. Udagawa, J. Electron Spectrosc. Relat. Phenom. **112**, 107 (2000).

[38] http://www.roentdek.com/ (unpublished).

[39] M. Inokuti, Rev. Mod. Phys. **43**, 297 (1971).

[40] K. T. Leung, J. Electron Spectrosc. Relat. Phenom. **100**, 237 (1999).

[41] M. E. Rose, *Elementary Theory of Angular Momentum* (Wiley, New York, 1957).

[42] J. Rolke, Y. Zheng, C. E. Brion, Y. A. Wang, and E. R. Davidson, Chem. Phys. **230**, 153 (1998).

[43] J. A. R. Samson, G. H. Rayborn, and P. N. Pareek, J. Chem. Phys. **76**, 393 (1982).

[44] K. Takeshita, Y. Sadamatu, and K. Tanaka, J. Chem. Phys. **122**, 044302 (2005).

[45] P. Lin and R. R. Lucchese, J. Chem. Phys. **116**, 8863 (2002).

[46] P. Baltzer, B. Wannberg, L. Karlsson, M. C. Göthe, and M. Larsson, Phys. Rev. A **45**, 4374 (1992).

[47] N. Watanabe, T. Hirayama, D. Suzuki and M. Takahashi, J. Chem. Phys. **138**, 184311 (2013).

[48] J. S. Lee, J. Chem. Phys. **67**, 3998 (1977).

[49] Y. Hikosaka, T. Aoto, R. I. Hall, and K. Ito, J. Phys. B: At. Mol. Opt. Phys. **36**, 1423 (2003).

[50] D. M. P. Holland and D. A. Shaw, Chem. Phys. **409**, 11 (2012).

[51] Y. Hikosaka, P. Lablanquie, M. Ahmad, R. I. Hall, J. G. Lambourne, F. Penent, and J. H. D. Eland, J. Phys. B: At. Mol. Opt. Phys. **36**, 4311 (2003).

[52] F. V. Demekhin, D. V. Omelýanenko, B. M. Lagutin, V. L. Sukhorukov, L. Werner, A. Ehresmann, K.-H. Schartner, and H. Schmoranzer, Rus. J. Phys. Chem. B **1**, 213 (2007).